Revision 1

A Grüneisen tensor for rutile and its application to host-inclusion systems

Word count: 4914

Kira A. Musiyachenko[1], Mara Murri[2], Mauro Prencipe[3], *Ross J. Angel[4], Matteo Alvaro[1]

[1]*Department of Earth and Environmental Sciences, University of Pavia, Via A. Ferrata, 1 27100 Pavia, Italy*
[2]*Department of Earth and Environmental Sciences, University of Milano-Bicocca, Piazza della Scienza 4, I-20126 Milano, Italy*
[3]*Department of Earth Sciences, University of Torino, Via Valperga Caluso 35, 10125 Torino, Italy*
[4] *IGG CNR, Via Giovanni Gradenigo, 6, 35131 Padova, Italy*

*Corresponding author: ross.angel@igg.cnr.it

Submitted to American Mineralogist

Abstract

Rutile is often found as inclusions in garnet, quartz and several other rock-forming minerals and it is also a common accessory phase in high-pressure metamorphic rocks. Its relatively simple structure, chemistry, broad PT stability field and its wide occurrence in nature makes it a candidate for the application of elastic geobarometry. However, thermodynamic studies coupled with observations on natural samples predict that rutile inclusions in garnets should exhibit zero residual pressure. This implies that the rutile inclusions are detached from the inclusion walls in the host garnet after entrapment. We determined the elastic and vibrational properties of rutile via ab initio hybrid Hartree Fock/Density Functional Theory simulations under different strain states. Our results confirmed the thermodynamic behavior of rutile in garnet and allowed us to determine for the first time the components of the phonon-mode Grüneisen tensors of rutile. We demonstrated that pure rutile inclusions in garnets from metamorphic rocks exhibit no residual strain or stress,

consistent with thermodynamic modelling. Nevertheless, there are rutile inclusions in garnet surrounded by optical birefringence haloes, which are indicative of residual inclusion pressures. Careful examination of these show that they contain significant amounts of amphibole which reduce the elastic moduli of the composite inclusion to less than that of the garnet hosts. A calculation method for the residual pressures of multi-phase inclusions is described.

Keywords: rutile, Grüneisen tensor, HF/DFT, elastic geobarometry

Introduction

Rutile is a widely distributed mineral in all types of rocks and has a wide range of applications in Earth sciences. It is one of the most important carriers of titanium and high field strength elements (HFSEs: Nb, Ta, Zr, Hf) (e.g. Meinhold 2010). Large rutile crystals usually occur in granitic pegmatites and vein mineralization (e.g. Černý et al. 2007, 2015). More commonly, rutile occurs as an accessory phase, both as inclusions in the rock-forming minerals and within the matrix. Rutile inclusions can have several origins; they can be primary (i.e. igneous or metamorphic, peritectic, xenocrystic) or secondary phases (i.e. hydrothermal alteration, e.g. Carruzzo et al. 2006; Meinhold 2010).

Rutile is already widely used in classical geothermobarometry in a variety of chemical thermometers and barometers (e.g. Ferry and Watson 2007). Moreover, when it occurs as primary inclusions, it also has the potential to provide fundamental information about the pressures and temperatures of entrapment through elastic geobarometry. This provides a different and complementary approach to recover the crystallization conditions of the system which does not require a chemical equilibrium, but it is based on the elastic interactions between the host –

inclusion pair (e.g. Rosenfeld and Chase 1961; Angel et al. 2014b; Alvaro et al. 2020). Because of the contrast in the elastic properties, the host-inclusion system develops non-lithostatic stresses upon exhumation. The residual elastic strain in the inclusion can be determined directly (e.g. from the measured lattice parameters with single-crystal X-ray diffraction) or indirectly from the changes in the wavenumbers of Raman-active phonon modes relative to an unstrained crystal with the phonon-mode Grüneisen approach (Murri et al. 2018; Angel et al. 2019). The remnant inclusion stress is then calculated from the measured strains. In addition, the remnant stress in the inclusion can be detected as birefringence haloes around the inclusion pointing to the fact that the host-inclusion interface and the surrounding host mineral is deformed (i.e. it is subject to strains, Campomenosi et al. 2020).

In this paper we present the structure and the Raman spectra of rutile calculated by means of ab initio hybrid Hartree-Fock/Density Functional Theory (HF/DFT) simulations under different strain conditions (i.e. from -2% to +2% covering the expected range of strains for common rutile inclusions) in order to determine the components of the phonon-mode Grüneisen tensors of rutile. We then discuss the application of elastic geobarometry to garnet-rutile host-inclusion systems.

Methods

Quantum mechanical calculations

Ab initio hybrid HF/DFT simulations have been performed with the CRYSTAL17 code (Dovesi et al. 2018b) by employing the WC1LYP functional which is particularly suitable for the correct reproduction of the elastic and vibrational properties of crystals (e.g. Prencipe 2012, 2019; Stangarone et al. 2016). The WC1LYP functional is based on the generalized gradient approximation (GGA) exchange functional WC (Wu and Cohen 2006), mixed with 16% of the

exact non-local Hartree–Fock exchange. The functional also includes the LYP correlation contribution (Lee et al. 1988). The grid for the numerical evaluation of the DFT exchange–correlation functionals was chosen by the keyword XXLGRID of the CRYSTAL17 user manual (Dovesi et al. 2018a) and corresponds to a total of 19394 points in the unit cell. A measure of the numerical accuracy provided by such a grid is the evaluation of the total number of electrons in the unit cell, by the numerical integration of the electron density over the cell volume. For rutile, we obtained 76.00003 electrons out of 76 for the reference volume at the static limit (i.e. 0 GPa and no zero-point and thermal pressures due to vibrational effects included; see Prencipe et al. 2011). The localized contracted atomic basis sets used were 8-6411(d311f) and 8-411d11f (Erba and Dovesi 2013; Peintinger et al. 2013) for Ti and O, respectively.

Within the CRYSTAL code, the accuracy in evaluating the Coulomb and Hartree–Fock exchange series is controlled by the keyword TOLINTEG, for which we set the five parameters to 10 (T1, T2, T3 and T4) and 24 (T5) (Dovesi et al. 2014). The diagonalization of the Hamiltonian matrix was performed at 18 independent k vectors in reciprocal space (Monkhorst and Pack 1976) by setting the shrinking factor IS to 4 (Dovesi et al. 2014). Cell parameters and fractional coordinates were optimized by analytical gradient methods, as implemented in CRYSTAL17 (Civalleri et al. 2001; Dovesi et al. 2014; Dovesi et al. 2018b). For hydrostatic simulations, lattice parameters and fractional coordinates were optimized at the WC1LYP level (at the static limit), at pressures of 0, 3, 5 and 10 GPa using the keyword EXTPRESS. Geometry optimization was considered converged when each component of the gradient (TOLDEG parameter in CRYSTAL17) was smaller than 0.00003 Hartree/ Bohr and displacements (TOLDEX) were smaller than 0.00012 Bohr with respect to the previous step. For the non-hydrostatic simulations, the cell was fixed at the chosen strain conditions and only the fractional coordinates were optimized with the keyword

ATOMONLY (Civalleri et al. 2001; Dovesi et al. 2014). The chosen values of strains are large enough to provide changes in frequency of vibrational modes that are significantly above the level of the numerical noise in the simulations. These values also cover the range of strains expected to be found in rutile inclusions. All simulations preserved the tetragonal symmetry of rutile. Vibrational wavenumbers of all of the normal modes were calculated at the Γ point within the limit of the harmonic approximation, by diagonalizing a mass-weighted Hessian matrix, whose elements are the second derivatives of the full potential of the crystal with respect to the mass-weighted atomic displacements (Pascale et al. 2004).

Structural and vibrational data for all of the simulations, performed at the static limit, are reported in the deposited crystallographic information file (cif). The space group symmetry of rutile, TiO_2, is $P4_2/mnm$ with a primitive unit cell containing 6 atoms. This gives rise to 18 crystal normal phonons in rutile, three of which are acoustic phonons and have zero wavenumber at the Brillouin-zone center. Hence, the representation of the remaining 15 optic phonons at the center of the Brillouin zone is:

$$\Gamma_{opt} = 1A_{1g}+1A_{2g}+1A_{2u}+ 1B_{1g}+1B_{2g}+2B_{1u}+1E_g+3E_u$$

The A_{2g}, A_{2u}, B_{1u} and E_u modes are only infrared-active, while the A_{1g} mode is non-polar and only Raman active together with the B_{1g}, B_{2g} and the doubly degenerate E_g mode. Since rutile is centrosymmetric the transverse and longitudinal optical polarizations of the E_g mode have the same frequency.

Raman spectroscopy

Rutile Raman spectra of both intergranular grains and inclusions in garnet were collected from eclogite sample SL501 from Pohorje Mountains (Eastern Alps, Slovenia, Vrabec et al. 2012). Two

115 reference rutile crystals were measured as standards. One intergranular rutile was measured to
116 have a reference with the same chemical composition as the inclusions. A further crystal of
117 unknown provenance was selected from the mineralogical collection of the Department of Earth
118 and Environmental Sciences at the University of Pavia to have another standard free crystal of
119 rutile.

120 Raman spectra were collected with a Horiba LabRam HR Evolution spectrometer (holographic
121 gratings of 1800 grooves/mm) equipped with an Olympus BX41 confocal microscope at the
122 controlled temperature of 20(1)°C. Raman spectra were excited by the 532 nm line of a solid state
123 (YAG) laser. The laser power on the sample surface was approximately 1-2 mW. The spectrometer
124 was calibrated to the silicon Raman peak at 520.5 cm^{-1}. The spectral resolution was ~ 2 cm^{-1} and
125 the instrumental reproducibility in determining the peak positions was ~ 0.5 cm^{-1}. The OriginPro®
126 2018 software package was used for data evaluation. The collected spectra were baseline corrected
127 for the continuum luminescence background and normalized to the acquisition time. Peak
128 positions, full-widths at half maximum (FWHMs), and integrated intensities were determined from
129 fits with pseudo-Voigt functions [pV=(1-q)*Lorentz+q*Gauss, where q is the weight coefficient].
130 The change in the peak position, hereafter $\Delta\omega$ (cm^{-1}), is calculated as the difference between the
131 wavenumber of the peak of the sample inclusion crystal (ω_i) and the peak position of the unstrained
132 reference crystal (ω_0) used as the standard. To avoid changes in peak position due to instrumental
133 drift and/or minor changes to room temperature affecting $\Delta\omega$, the unstrained standard of the rutile
134 was measured multiple times per session. The ω_0 values were averaged and then subtracted from
135 the ω_i of the strained inclusions analyzed in between two consecutive standard measurements to
136 obtain $\Delta\omega$.

137 ## Results

Structure at the static limit

The structure of rutile consists of chains of TiO_6 octahedra parallel to **c** axis (Fig. 1). Each chain is built by octahedra each of which shares two opposite edges with adjacent octahedra. The structure has one unique titanium and oxygen position and two non-equivalent nearest neighbor Ti-O distances with the longer two (Ti-O_b) oriented perpendicular to the **c**-axis and the shorter four Ti-O_a lying in the <110> plane. Lattice and structural parameters (atomic coordinates, bonds and angles, Table 1) determined via ab initio simulations at the static limit (0 K, 0 GPa static pressure) are in good agreement with those from Burdett et al. (1987) determined by neutron diffraction measurements at 15K (Table 1, column "tw-b" – the difference between the results of this work and the results of Burdett et al. (1987), columns "this work" and "b" respectively).

Hydrostatic calculations of the lattice parameters (V/V_0, a/a_0, c/c_0) reproduced correctly the pattern of anisotropy of the elasticity of rutile, with the **c**-axis being much stiffer than the **a** and **b**-axes (Fig. 2b,c). The zero-pressure bulk modulus determined by fitting the volumes from the hydrostatic simulations against static pressures with a 3rd order Birch-Murnaghan equation of state (BM3-EoS), is 233.78(24) GPa with the $K' = 4.54(5)$. The calculated bulk modulus is stiffer than that determined by Zaffiro et al. (2019) and Angel et al. (2020) from the available data in the literature (K_{0T} = 205.14(15) GPa, K'=6.9(4)), obtained by using the same EoS, partially because our simulations are performed at the static limit and therefore do not account either for the zero-point pressure nor for thermal pressure that would soften the bulk modulus on passing from 0K to 300K (Prencipe et al. 2011). In addition, the rutile structure has a soft mode whose effect on the bulk modulus will not be accounted for in our static DFT simulations. The intrinsic anharmonicity of the soft mode would cause a further reduction of the calculated K_{0T}. This effect was observed for the soft mode in quartz (e.g. Demuth et al. 1999; Kimizuka et al. 2003).

Structure under various strain conditions

Under hydrostatic conditions the structures simulated by HF/DFT show a smooth compression of all structural parameters with increasing pressure (hydrostatic pressure trend is marked by the dotted line in Fig. 3). Figure 3 shows the change of various structural parameters of rutile under non-symmetry-breaking strains. The strain definition used is Lagrangian infinitesimal and the reference system for the strains coincides with the unit-cell axes. Therefore, $\varepsilon_3 = \frac{c}{c_0} - 1$ represents the fractional change of the **c** axis relative to the unstrained reference state at zero pressure, with cell parameters a_0 and c_0. To maintain tetragonal symmetry, the strains ε_1 and ε_2 were constrained to be equal, and the contour maps are therefore plotted with $2\varepsilon_1=\varepsilon_1+\varepsilon_2$ as the *x*-axis. A negative strain therefore corresponds to a compression of the corresponding axis, and the lower left quadrant of the contour plots represents compression of all three axes of the unit cell of rutile. The top left quadrant represents conditions of shear strain, equivalent to expansion of the **c** axis and isotropic compression in the **a-b** plane. The bottom right quadrant represents the opposite sense of shear strains.

Shortening of the Ti-O bonds with negative ε_1 and ε_3 strains is explained by geometrical orientation of the bonds: Ti-O_b is parallel to the **a-b** plane while Ti-O_a has a smaller angle with the **c** axis (Fig. 1). In contrast values of the bond angles display a strong dependence on the deviatoric strain with the Ti-O-Ti(1) being the less sensitive, whereas polyhedral volume contours are parallel to the isochors (Fig. 3c). This pattern of structural behavior is similar to that of quartz and zircon (Murri et al. 2019; Stangarone et al. 2019), demonstrating that non-hydrostatic stresses in the most common mineral inclusions found in garnet hosts are mostly accommodated by internal angular distortion and deformation of the polyhedra (i.e. SiO_4 tetrahedra, ZrO_8 polyhedra and TiO_6 octahedra). These studies show that the dominant structural response of crystal structures under

184 deviatoric stress is shear deformation of the strongly bonded cation-oxygen polyhedra and, where
185 this is allowed by the topology of the structure, as in quartz (Murri et al. 2019), the tilting of the
186 polyhedra with respect to one another.

187 **Raman spectrum**

188 Experimentally-determined Raman spectra of rutile consist of four easily-detectable bands: one
189 low intensity sharp peak at 142 cm^{-1} (B_{1g}), a broad band centered at 230 cm^{-1} (multi-phonon
190 interaction process, Porto et al. 1967), a medium intensity band at 445 cm^{-1} (E_g) and a strong band
191 at 609 cm^{-1} (A_{1g}). Moreover, from the factor group analysis (see Methods section), one B_{2g} mode
192 is also Raman active. This occurs at 801 cm^{-1}, but it is usually hard to detect due to its very low
193 intensity and broad character (Fig. 4). On the other hand, while frequency calculations based on
194 the DFT simulations do not suffer detection limits due to weak intensities or broad peak widths as
195 do experiments, they do not include phonon-phonon interaction processes. Therefore, the broad
196 band at 230 cm^{-1} is not reported in the calculated Raman spectra. Calculated Raman frequencies
197 at the reference state (0 GPa static limit and 0 K) are reported in Table 2 together with the measured
198 Raman frequencies on our 'standard' rutile from Pohorje (peak positions of the two selected
199 standards are the same within the instrumental reproducibility of ~ 0.5 cm^{-1}) and literature data
200 which includes both theoretical and experimental data. Values of the calculated peak positions at
201 0K differ slightly from the experimental results at room temperature, due to the difference in
202 temperature and the specifics of the calculation method. Ab initio hybrid HF/DFT calculations
203 with the WC1LYP functional proved, on average, to be more effective in reproducing vibrational
204 frequencies than other methods (Prencipe 2012, 2019). Frequencies calculated with WC1LYP for
205 the E_g, A_{1g} and B_{2g} modes are all within the range of experimental uncertainty. The significant

206 discrepancy occurs with the experimental value of the B_{1g} mode because it is a low frequency
207 partially anharmonic mode, for which the computational uncertainties are larger.

208 Figure 5 displays the calculated $\Delta\omega$ (cm^{-1}) of the rutile Raman active modes (black solid lines) as
209 a function of the two independent strain components. The E_g, A_{1g} and B_{2g} modes display an
210 increase of their vibrational frequencies with increase of negative strains. Their behavior could be
211 seen to be almost linear within the studied strain field. According to the calculated displacement
212 vectors from the DFT simulations, the E_g mode involves the vibrations along the **c** axis of the O_b
213 atoms (Figure 1) with the O_a atoms remaining fixed (one of the possible displacement geometries).
214 The A_{1g} and the B_{2g} modes correspond to the movements of the oxygen atoms in the **a-b** planes
215 which includes Ti-O_b stretching and O_a-Ti-O_a scissoring in the <110> plane. The B_{1g} mode has an
216 opposite behavior with respect to all of the other modes in that it displays negative shifts under
217 compression (Fig. 5a). This anomalous behavior has already been described in the literature and
218 is related to the pressure-induced structural phase transitions in rutile (Samara and Peercy 1973).
219 The B_{1g} mode corresponds to rotational vibrations of the octahedra around the **c** axis. The
220 directions of the rotations between adjacent octahedra are opposite to one another so this mode
221 represents a distortion of the octahedral chains involving only oxygen atom motions in the **a-b**
222 plane. Softening of the B_{1g} optic mode drives a ferroelastic transition in which the symmetry is
223 reduced from $P4_2/mnm$ to *Pnnm* that also occurs at high pressures in several other compounds (e.g.
224 stishovite, Carpenter et al. 2000) that have the rutile structure type.

225 **Grüneisen tensor**

226 Since the contour lines of equal $\Delta\omega$ (cm^{-1}) (black solid lines in the plots in Fig. 5) are equally-
227 spaced, straight and parallel to one-another, the dependence of all of the Raman modes of rutile on
228 strain is linear. Therefore, the phonon-mode Grüneisen tensor approach can be applied in order to

229 determine the Grüneisen tensor components for each Raman active mode. These will allow the
230 strains in crystals to be determined from measured $\Delta\omega$ (cm^{-1}) and vice versa. The phonon-mode
231 Grüneisen tensor $\boldsymbol{\gamma^m}$ is a second rank symmetric property tensor (e.g. Ziman 1960; Key 1967;
232 Cantrell 1980; Angel et al. 2019) characteristic of each phonon mode *m.* Therefore, since only
233 non-symmetry-breaking strains are considered, it obeys the symmetry constraints of the studied
234 system. Rutile is tetragonal with non-symmetry-breaking strains restricted to $\varepsilon_1 = \varepsilon_2 \neq \varepsilon_3$ and, as a
235 consequence, there are only two symmetry-independent Grüneisen components to be determined
236 for each Raman active mode: γ_1^m and γ_3^m .Thus, the relationship between the wavenumber shifts
237 of the Raman modes of rutile and the strains can be written in terms of the Grüneisen tensor as:

238 $$-\frac{\Delta\omega}{\omega 0} = 2\gamma_1^m\varepsilon_1 + \gamma_3^m\varepsilon_3 \qquad (1)$$

239 We determined the phonon-mode Grüneisen tensor components γ_1^m and γ_3^m for each Raman-active
240 mode of rutile by a least-squares fit of the calculated $\Delta\omega$ (cm^{-1}) as a function of the strains. The
241 reference values of ω_0 were taken from our measurements on the standard intergranular rutile from
242 Pohorje (Slovenia).

243 In order to validate the calculated values of the symmetry-independent components of the mode
244 Grüneisen tensors we used them along with measured unit-cell strains under pressure to predict
245 the Raman shift changes under pressure (Figure 6). The available Raman data in the literature are
246 only presented in the form of pressure derivatives ($\Delta\omega/P$ coefficients) and not measurements of
247 individual data. The pressure interval of the experiments was 0-4 GPa (Nicol and Fong 1971;
248 Samara and Peercy 1973), and in one case up to 40 GPa (Arashi 1992), but with a pressure medium
249 of 4:1 methanol-ethanol mixture which is hydrostatic only up to 9.8 GPa (Angel et al. 2007). We
250 have a good agreement for the B_{1g} and A_{1g} modes and our calculations for the E_g mode are

consistent with the experimental work done by Arashi (1992) over the larger interval of pressure. The difference in behavior of the calculated E_g mode from the experimental data of Nicol and Fong (1971) and Samara and Peercy (1973) might be due to its broader character and lower intensity compared to that of the A_{1g} mode.

Moreover, a linear behavior of the Raman modes with hydrostatic pressure is assumed when constant $\Delta\omega/P$ coefficients are used. However, the vibrational frequencies do not depend on the pressure but on the strains (Key 1967) and in our work were found to be linear with volume. The pressure dependence of the volume of rutile is described by the non-linear Burch-Murnaghan equation of state of the third order (Zaffiro et al. 2019). Thus, fitting the $\Delta\omega$ (cm^{-1}) against pressure with a linear equation is not correct.

Discussion

Garnet is one of the most common host minerals for rutile and many other key inclusions such as quartz and zircon in metamorphic rocks. Quartz- and zircon-in-garnet elastic geobarometry has been successfully used to reconstruct *PT* histories of metamorphic rocks (e.g. Gonzalez et al. 2019; Alvaro et al. 2020). However, calculations based on the equations of state of garnet (Milani et al. 2015) and rutile indicate that rutile inclusions trapped inside garnets at typical metamorphic conditions should exhibit negative residual pressures when measured at room conditions provided they did not undergo some non-elastic process after entrapment (Zaffiro et al. 2019). Ab initio calculations did not reveal any anomalous behavior of the structure in the studied range of strains which could result in a deviation of the behavior described by the EoS, nor any non-linearity in the Grüneisen relationship between strains and Raman peak shifts (Eqn. 1).

EoS calculations are confirmed by Raman measurements on both natural and synthetic samples. Bonazzi et al. (2019) synthesized at 3 GPa and 775°C almost pure pyrope garnets with quartz and rutile inclusions. We performed Raman measurements on the rutile inclusions from these samples and according to these and our optical observations these synthetic rutile inclusions show no signs of residual pressure. Moreover, pyrope megablasts from the Dora Maira UHP locality (Chopin and Schertl 1999) are a good example of a natural garnet-rutile host inclusion system. Several rutile inclusions that are found in the same growth zones as coesite inclusions in these garnets do not show any sign of residual pressure: their Raman peaks are at the same wavenumbers as the free reference crystal and there is no evidence for optical birefringence halos in the surrounding garnet (N. Campomenosi, personal communication). These observations are consistent with our simulation results and the thermodynamic calculations and indicate that rather than exhibiting negative pressures, which would imply that the rutile inclusions are bound to the host garnet crystal and stretched by it, the rutile inclusions are detached from the inclusion walls in the host garnet.

However, there are some rutile inclusions that appear to exhibit signs of residual pressure. For example, rutile inclusions in garnet from an eclogite from the Pohorje HP locality (Slovenia) are surrounded by a clearly distinguishable birefringence halo (Fig. 7).

This halo reflects the elastic deformation of the host garnet in the immediate vicinity of the inclusion due to its elastic relaxation (Campomenosi et al. 2020). The phenomenon of relaxation develops as a result of the differences between the thermo-elastic properties of the host and inclusion phases that lead to the inclusion exhibiting a different pressure than the host. Therefore, birefringence haloes around these rutile inclusions when their host is at room pressure indicate that the inclusions are at some non-ambient pressure that cannot be caused solely by the contrast in elastic properties between rutile and garnet.

295 Optical and Raman spectroscopic studies of rutile inclusions in garnet from Pohorje revealed the
296 presence of small amphibole crystals attached to each of the rutiles surrounded by a birefringence
297 halo (e.g. Fig 7a,d). Amphibole occurs as laminar crystals wrapping rutile grains, which makes it
298 hard to detect and determine a volume fraction. Raman 3D imaging allowed us to estimate that an
299 average volume fraction of amphibole in the inclusions exhibiting birefringence haloes is between
300 15 and 30 % of the inclusion volume (rutile + amphibole) (Fig. 8). Electron microprobe analyses
301 confirmed that the amphibole composition is close to the cummingtonite end member (Table S1).
302 The room-pressure bulk modulus of cummingtonite (Holland and Powell 2011) is 70 GPa, which
303 is less than half the bulk modulus of pyrope. If the inclusion were pure amphibole it would
304 therefore exhibit a positive residual inclusion pressure (P_{inc}) when examined in our sections.

305 The elastic properties of mixed-phase inclusions have Reuss and Voigt bounds. We used the Reuss
306 approximation as we expect the two phases to be under the same pressure rather than the same
307 strain (Voigt approximation). The Reuss bulk modulus depends on the volume fractions x_1 and x_2
308 of both components:

309 $$K_{tot} = \left(\frac{x_1}{K_1} + \frac{x_2}{K_2}\right)^{-1} \qquad (2)$$

310 On this basis, the presence of at least 14% in volume of cummingtonite is enough to reduce the
311 bulk modulus (at ambient conditions) of the mixture to less than that of the garnet (Fig 9). This
312 makes the inclusion softer than the host and should lead to the development of a positive inclusion
313 pressure upon exhumation.

314 The value of the relaxed inclusion pressure for the multiple phase inclusion can be calculated using
315 various approaches, for example an average EoS weighted by molar fractions. But this method is
316 inappropriate for the phases with contrasting elastic properties like rutile and amphibole because

317 it does not account correctly for the differences in K' between the phases. Therefore, we developed
318 a methodology that is implemented in the MPHASE utility of EosFit7c (Angel et al. 2014a), in
319 which the volume of the mixture at all P and T is treated as the sum of the volumes of the individual
320 phases calculated from their EoS weighted by their molar fractions. This calculation therefore
321 treats the inclusion as a closed system of fixed composition under uniform stress. The orange and
322 green curves in Figure 9 show variation of the P_{inc} value over the range of all possible amphibole
323 fractions in a cummingtonite+rutile inclusion for the entrapment conditions of 3 GPa 800°C and 2
324 GPa 600°C. Different entrapment conditions within the range of regional metamorphism lead to a
325 different slope of this curve, but it always crosses the point of zero P_{inc} at approximately 0.14
326 volume fraction of the amphibole component. A mixture of ~14 volume % of an cummingtonite
327 and ~86 % of a rutile has the same bulk modulus as a pyrope garnet, therefore P_{inc} should be
328 approximately zero in the interval from 13 to 15 vol.% of cummingtonite (variation of 1 vol.% for
329 the different entrapment conditions). Inverse calculations of the entrapment conditions of such
330 composite inclusions therefore require a precise measurement of the volume fractions of the phases
331 and the value of the P_{inc}, as well as the composition of the amphibole as the bulk modulus and EoS
332 of amphiboles varies with composition.

333 The multiphase inclusion from Pohorje eclogite with 30 vol.% of cummingtonite amphibole can
334 exhibit up to 0.28 GPa of a residual pressure according to the calculated P_{inc} curves, which is
335 consistent with the presence of birefringence haloes in the host around these inclusions. Changes
336 in the Raman peak positions ($\Delta\omega$, cm^{-1}) in the rutile spectrum corresponding to this pressure
337 however are impossible to resolve as they are less than the typical measurement uncertainties.
338 However, amphibole Raman $\Delta\omega$ (cm^{-1}) could be used to detect the residual pressure but for this a
339 reliable pressure calibration is needed.

Implications

Ab initio calculations of elastic and vibrational properties of rutile predicted a linear response of its structural parameters and vibrational frequencies to strains. We determined the symmetry-independent components of the phonon-mode Grüneisen tensors for the rutile Raman active modes that can be used in Raman elastic geobarometry calculations. Our DFT calculations succeeded in predicting the anomalous behavior of the soft B_{1g} mode. Thus, we confirm that a compressional strain causes a negative shift of the lowest-frequency Raman mode (141.6 cm^{-1}) of rutile.

Thermodynamic calculations predict a negative P_{inc} for rutile inclusions entrapped in garnet at H*P* conditions, therefore we would expect a positive peak shift for the B_{1g} mode and negative peak shifts for the other Raman modes in rutile. However, this behavior has not been observed so far, and pure rutile inclusions have zero pressures in both natural and synthetic samples. On the other hand, we demonstrated that detecting a positive P_{inc} in some rutile inclusions is theoretically possible due to softening of the overall inclusion bulk modulus. Extensive radiation damage to rutile or the presence of a second phase, softer than rutile and garnet (e.g. amphibole), can modify the bulk modulus of the inclusion enough to reverse the contrast of elastic properties to the host garnet. Here, we described a method to calculate the elastic properties of multiphase inclusions with the EoSFit-7c software (Angel et al. 2014a). The results of our calculations can be used as a control for the presence of plastic deformation, radiation damage or the vicinity of another phase in case where a residual pressure in the inclusion or a birefringence halo is detected.

Elastic geobarometry can still be used for rutile inclusions in other hosts with more contrasting elastic properties such as quartz or diamond (Angel et al. 2015, 2017). Even though quartz is softer than rutile at room *P* and *T*, a window of positive P_{inc} occurs for rutile inclusions entrapped at low

362 *P* (up to 0.7 GPa) and medium-high *T* (200-700 °C) conditions under the zero-pressure entrapment
363 isomeke (Fig. S1a). Rutile inclusions in diamond will exhibit positive P_{inc} if entrapped above the
364 zero isomeke (Fig. S1b) corresponding to low *T* and high *P* conditions. For example, a P_{inc} of 1
365 GPa, corresponding to a 0.4 % volume strain, will cause the Raman modes B_{1g}, E_g, A_{1g} and B_{2g} to
366 shift -3.2, 3.1, 4.2 and 5.2 cm^{-1}, respectively. These Δω values are significantly above the
367 measurement uncertainties caused by line broadening and thus residual pressures of rutile
368 inclusions in diamonds could be detected by Raman measurements.

369 In cases of a positive inclusion pressure, a strained rutile inclusion will display a negative $\Delta\omega$ cm^{-1}
370 for the B_{1g} mode and positive $\Delta\omega$ cm^{-1} for the other Raman modes. However, it is important to
371 remember that in anisotropic hosts the differences from the hydrostatic calibration depend on the
372 reciprocal orientation of host and inclusion. The problem of orientation is partially solved in case
373 of rutile inclusions that have exsolved from the host phase. They are usually tiny needles of
374 acicular rutile, oriented along crystallographic axes of the host phase. The process of the
375 decomposition of a Ti-rich solid solution leads to the formation of coherent inclusions (e.g. Zhang
376 et al. 2003; Proyer et al. 2013). Understanding the influence of this coherency on the resulting
377 strains in a host-inclusion system is now possible with an application of these newly calculated
378 symmetry-independent components of the phonon-mode Grüneisen tensors.

379 ## Acknowledgments

380 This project received funding from the European Research Council under the European Union's
381 Horizon 2020 research and innovation program grant agreement 714936 TRUE DEPTHS to
382 Matteo Alvaro. The authors thank Hugo Van Schrojenstein Lantman for the samples from Pohorje

383 and electron microprobe analyses, and Mattia Bonazzi and Nicola Campomenosi for discussions
384 about Raman data of rutile inclusions in garnet.

References

Abrahams, S.C., and Bernstein, J.L. (1971) Rutile: Normal Probability Plot Analysis and Accurate Measurement of Crystal Structure. The Journal of Chemical Physics, 55, 3206–3211.

Alvaro, M., Mazzucchelli, M.L., Angel, R.J., Murri, M., Campomenosi, N., Scambelluri, M., Nestola, F., Korsakov, A., Tomilenko, A.A., Marone, F., and others (2020) Fossil subduction recorded by quartz from the coesite stability field. Geology, 48, 24–28.

Angel, R.J., Bujak, M., Zhao, J., Gatta, G.D., and Jacobsen, S.D. (2007) Effective hydrostatic limits of pressure media for high-pressure crystallographic studies. Journal of Applied Crystallography, 40, 26–32.

Angel, R.J., Alvaro, M., and Gonzalez-Platas, J. (2014a) EosFit7c and a Fortran module (library) for equation of state calculations. Zeitschrift für Kristallographie - Crystalline Materials, 229, 405–419.

Angel, R.J., Mazzucchelli, M.L., Alvaro, M., Nimis, P., and Nestola, F. (2014b) Geobarometry from host-inclusion systems: The role of elastic relaxation. American Mineralogist, 99, 2146–2149.

Angel, R.J., Alvaro, M., Nestola, F., and Mazzucchelli, M.L. (2015) Diamond thermoelastic properties and implications for determining the pressure of formation of diamond-inclusion systems. Russian Geology and Geophysics, 56, 211–220.

Angel, R.J., Alvaro, M., Miletich, R., and Nestola, F. (2017) A simple and generalised P–T–V EoS for continuous phase transitions, implemented in EosFit and applied to quartz. Contributions to Mineralogy and Petrology, 172, 29.

Angel, R.J., Murri, M., Mihailova, B., and Alvaro, M. (2019) Stress, strain and Raman shifts. Zeitschrift für Kristallographie - Crystalline Materials, 234, 129–140.

Angel, R.J., Alvaro, M., Schmid-Beurmann, P., and Kroll, H. (2020) Commentary on "Constraints on the Equations of State of stiff anisotropic minerals: rutile, and the implications for rutile elastic barometry" [Miner. Mag. 83 (2019) pp. 339–347]. Mineralogical Magazine, 84, 339–347.

Arashi, H. (1992) Raman spectroscopic study of the pressure-induced phase transition in TiO_2. Journal of Physics and Chemistry of Solids, 53, 355–359.

Bonazzi, M., Tumiati, S., Thomas, J.B., Angel, R.J., and Alvaro, M. (2019) Assessment of the reliability of elastic geobarometry with quartz inclusions. Lithos, 350–351, 105201.

Burdett, J.K., Hughbanks, T., Miller, G.J., Richardson, J.W., and Smith, J.V. (1987) Structural-electronic relationships in inorganic solids: powder neutron diffraction studies of the rutile and anatase polymorphs of titanium dioxide at 15 and 295 K. Journal of the American Chemical Society, 109, 3639–3646.

Campomenosi, N., Mazzucchelli, M.L., Mihailova, B., Scambelluri, M., Angel, R.J., Nestola, F., Reali, A., and Alvaro, M. (2018) How geometry and anisotropy affect residual strain in host-inclusion systems: Coupling experimental and numerical approaches. American Mineralogist, 103, 2032–2035.

Campomenosi, N., Mazzucchelli, M.L., Mihailova, B.D., Angel, R.J., and Alvaro, M. (2020) Using polarized Raman spectroscopy to study the stress gradient in mineral systems with anomalous birefringence. Contributions to Mineralogy and Petrology, 175, 16.

Cantrell, J.H. (1980) Generalized Grüneisen tensor from solid nonlinearity parameters. Physical Review B, 21, 4191–4195.

Carpenter, M.A., Hemley, R.J., and Mao, H. (2000) High-pressure elasticity of stishovite and the $P4_2/mnm \rightleftharpoons Pnnm$ phase transition. Journal of Geophysical Research: Solid Earth, 105, 10807–10816.

Carruzzo, S., Clarke, D.B., Pelrine, K.M., and MacDonald, M.A. (2006) Texture, composition, and origin of rutile in the South Mountain batholith, Nova Scotia. The Canadian Mineralogist, 44, 715–729.

Černý, P., Novak, M., Chapman, R., and Ferreira, K.J. (2007) Subsolidus behavior of niobian rutile from the Pisek region, Czech Republic: a model for exsolution in W^{-} and $Fe^{2+}>>Fe^{3+}$-rich phases. Journal of Geosciences, 52, 143–159.

Černý, P., Chapman, R., Simmons, W.B., and Chackowsky, L.E. (2015) Niobian rutile from the McGuire granitic pegmatite, Park County, Colorado: Solid solution, exsolution, and oxidation. American Mineralogist, 84, 754–763.

Chopin, C., and Schertl, H.-P. (1999) The UHP Unit in the Dora-Maira Massif, Western Alps. International Geology Review, 41, 765–780.

Civalleri, B., D'Arco, Ph., Orlando, R., Saunders, V.R., and Dovesi, R. (2001) Hartree–Fock geometry optimisation of periodic systems with the Crystal code. Chemical Physics Letters, 348, 131–138.

Demuth, T., Jeanvoine, Y., Hafner, J., and Ángyán, J.G. (1999) Polymorphism in silica studied in the local density and generalized-gradient approximations. Journal of Physics: Condensed Matter, 11, 3833–3874.

Dovesi, R., Saunders, V.R., Roetti, C., Orlando, R., Zicovich Wilson, C.M., Pascale, F., Civalleri, B., Doll, K., Harrison, N.M., Bush, I.J., and others (2014) CRYSTAL14.

Dovesi, Roberto, Saunders, V.R., Roetti, C., Orlando, R., Zicovich-Wilson, C.M., Pascale, F., Civalleri, B., Doll, K., Harrison, N.M., Bush, I.J., and others (2018) CRYSTAL17 User's Manual, 461 p.

Dovesi, R., Erba, A., Orlando, R., Zicovich-Wilson, C.M., Civalleri, B., Maschio, L., Rérat, M., Casassa, S., Baima, J., Salustro, S., and others (2018) Quantum-mechanical condensed matter simulations with CRYSTAL. WIREs Computational Molecular Science, 8, 1360.

Erba, A., and Dovesi, R. (2013) Photoelasticity of crystals from theoretical simulations. Physical Review B, 88, 045121.

Ferry, J.M., and Watson, E.B. (2007) New thermodynamic models and revised calibrations for the Ti-in-zircon and Zr-in-rutile thermometers. Contributions to Mineralogy and Petrology, 154, 429–437.

Gonzalez, J.P., Thomas, J.B., Baldwin, S.L., and Alvaro, M. (2019) Quartz-in-garnet and Ti-in-quartz thermobarometry: Methodology and first application to a quartzofeldspathic gneiss from eastern Papua New Guinea. Journal of Metamorphic Geology, 37, 1193–1208.

Henderson, C.M.B., Knight, K.S., and Lennie, A.R. (2009) Temperature dependence of rutile (TiO_2) and geikielite ($MgTiO_3$) structures determined using neutron powder diffraction. The Open Mineralogy Journal, 3, 1–11.

Holland, T.J.B., and Powell, R. (2011) An improved and extended internally consistent thermodynamic dataset for phases of petrological interest, involving a new equation of state for solids. Journal of Metamorphic Geology, 29, 333–383.

Key, S.W. (1967) Grüneisen Tensor for Anisotropic Materials. Journal of Applied Physics, 38, 2923–2928.

Kimizuka, H., Kaburaki, H., and Kogure, Y. (2003) Molecular-dynamics study of the high-temperature elasticity of quartz above the \ensuremath{\alpha}-\ensuremath{\beta} phase transition. Physical Review B, 67, 024105.

Lan, T., Tang, X., and Fultz, B. (2012) Phonon anharmonicity of rutile TiO_2 studied by Raman spectrometry and molecular dynamics simulations. Physical Review B, 85, 094305.

Lan, T., Li, C.W., Hellman, O., Kim, D.S., Muñoz, J.A., Smith, H., Abernathy, D.L., and Fultz, B. (2015) Phonon quarticity induced by changes in phonon-tracked hybridization during lattice expansion and its stabilization of rutile TiO_2. Physical Review B, 92, 054304.

Lee, C., Yang, W., and Parr, R.G. (1988) Development of the Colle-Salvetti correlation-energy formula into a functional of the electron density. Physical Review B, 37, 785–789.

Meinhold, G. (2010) Rutile and its applications in earth sciences. Earth-Science Reviews, 102, 1–28.

Merle, P., Pascual, J., Camassel, J., and Mathieu, H. (1980) Uniaxial-stress dependence of the first-order Raman spectrum of rutile. I. Experiments. Physical Review B, 21, 1617–1626.

Milani, S., Nestola, F., Alvaro, M., Pasqual, D., Mazzucchelli, M.L., Domeneghetti, M.C., and Geiger, C.A. (2015) Diamond–garnet geobarometry: The role of garnet compressibility and expansivity. Lithos, 227, 140–147.

Mitev, P.D., Hermansson, K., Montanari, B., and Refson, K. (2010) Soft modes in strained and unstrained rutile TiO_2. Physical Review B, 81, 134303.

Momma, K., and Izumi, F. (2008) VESTA: a three-dimensional visualization system for electronic and structural analysis. Journal of Applied Crystallography, 41, 653–658.

Monkhorst, H.J., and Pack, J.D. (1976) Special points for Brillouin-zone integrations. Physical Review B, 13, 5188–5192.

Montanari, B., and Harrison, N.M. (2002) Lattice dynamics of TiO_2 rutile: influence of gradient corrections in density functional calculations. Chemical Physics Letters, 364, 528–534.

Murri, M., Mazzucchelli, M.L., Campomenosi, N., Korsakov, A.V., Prencipe, M., Mihailova, B.D., Scambelluri, M., Angel, R.J., and Alvaro, M. (2018) Raman elastic geobarometry for anisotropic mineral inclusions. American Mineralogist, 103, 1869–1872.

Murri, M., Alvaro, M., Angel, R.J., Prencipe, M., and Mihailova, B.D. (2019) The effects of non-hydrostatic stress on the structure and properties of alpha-quartz. Physics and Chemistry of Minerals, 46, 487–499.

Nicol, M., and Fong, M.Y. (1971) Raman spectrum and polymorphism of titanium dioxide at high pressures. The Journal of Chemical Physics, 54, 3167–3170.

Pascale, F., Zicovich-Wilson, C.M., Gejo, F.L., Civalleri, B., Orlando, R., and Dovesi, R. (2004) The calculation of the vibrational frequencies of crystalline compounds and its implementation in the CRYSTAL code. Journal of Computational Chemistry, 25, 888–897.

Peintinger, M.F., Oliveira, D.V., and Bredow, T. (2013) Consistent Gaussian basis sets of triple-zeta valence with polarization quality for solid-state calculations. Journal of Computational Chemistry, 34, 451–459.

Porto, S.P.S., Fleury, P.A., and Damen, T.C. (1967) Raman Spectra of TiO_2, MgF_2, ZnF_2, FeF_2, and MnF_2. Physical Review, 154, 522–526.

Prencipe, M. (2012) Simulation of vibrational spectra of crystals by ab initio calculations: an invaluable aid in the assignment and interpretation of the Raman signals. The case of jadeite ($NaAlSi_2O_6$). Journal of Raman Spectroscopy, 43, 1567–1569.

——— (2019) Quantum mechanics in Earth sciences: a one-century-old story. Rendiconti Lincei. Scienze Fisiche e Naturali, 30, 239–259.

Prencipe, M., Scanavino, I., Nestola, F., Merlini, M., Civalleri, B., Bruno, M., and Dovesi, R. (2011) High-pressure thermo-elastic properties of beryl ($Al_4Be_6Si_{12}O_{36}$) from ab initio

calculations, and observations about the source of thermal expansion. Physics and Chemistry of Minerals, 38, 223–239.

Proyer, A., Habler, G., Abart, R., Wirth, R., Krenn, K., and Hoinkes, G. (2013) TiO2 exsolution from garnet by open-system precipitation: evidence from crystallographic and shape preferred orientation of rutile inclusions. Contributions to Mineralogy and Petrology, 166, 211–234.

Rosenfeld, J.L., and Chase, A.B. (1961) Pressure and temperature of crystallization from elastic effects around solid inclusions in minerals? American Journal of Science, 259, 519–541.

Samara, G.A., and Peercy, P.S. (1973) Pressure and Temperature Dependence of the Static Dielectric Constants and Raman Spectra of TiO_2 (Rutile). Physical Review B, 7, 1131–1148.

Stangarone, C., Tribaudino, M., Prencipe, M., and Lottici, P.P. (2016) Raman modes in Pbca enstatite ($Mg_2Si_2O_6$): an assignment by quantum mechanical calculation to interpret experimental results. Journal of Raman Spectroscopy, 47, 1247–1258.

Stangarone, C., Angel, R.J., Prencipe, M., Campomenosi, N., Mihailova, B., and Alvaro, M. (2019) Measurement of strains in zircon inclusions by Raman spectroscopy. European Journal of Mineralogy, 685–694.

Sugiyama, K., and Takéuchi, Y. (2015) The crystal structure of rutile as a function of temperature up to 1600° C. Zeitschrift für Kristallographie - Crystalline Materials, 194, 305–314.

Vrabec, M., Janák, M., Froitzheim, N., and De Hoog, J.C.M. (2012) Phase relations during peak metamorphism and decompression of the UHP kyanite eclogites, Pohorje Mountains (Eastern Alps, Slovenia). Lithos, 144–145, 40–55.

Wu, Z., and Cohen, R.E. (2006) More accurate generalized gradient approximation for solids. Physical Review B, 73, 235116.

Zaffiro, G., Angel, R.J., and Alvaro, M. (2019) Constraints on the Equations of State of stiff anisotropic minerals: rutile, and the implications for rutile elastic barometry. Mineralogical Magazine, 83, 339–347.

Zhang, R.Y., Zhai, S.M., Fei, Y.W., and Liou, J.G. (2003) Titanium solubility in coexisting garnet and clinopyroxene at very high pressure: the significance of exsolved rutile in garnet. Earth and Planetary Science Letters, 216, 591–601.

Ziman, J.M. (1960) Electrons and Phonons, the International Series of Monographs on Physics. Oxford University, London, UK.

List of figure captions

Figure 1. Rutile structure model in three dimensions. Blue spheres in octahedral coordination represent Ti atoms, red spheres represent O atoms. Bonds are represented by dark-gray lines. The unit cell of rutile is indicated by the dashed lines. Structure was drawn with the VESTA software (Momma and Izumi 2008) based on the ab initio calculation at the static limit

Figure 2. Lattice parameters and volume of rutile as a function of pressure.

Figure 3. Contour maps of structural parameters of rutile as a function of strains e1 and e3. Strains derived from the hydrostatic pressure simulations lie along the dotted line and represent pressure conditions of 0, 1, 3, 5, and 10 GPa; zero pressure is at the origin of all of these plots.

Figure 4. Raman spectra of the two natural rutile samples used as standards (rutile standard free crystal and intergranular rutile standard from the Pohorje eclogite).

Figure 5. Calculated wavenumber shifts (cm^{-1}) of the Raman-active modes of rutile. Strains derived from the hydrostatic pressure simulations lie along the dotted line and represent pressure conditions of 0, 1, 3, 5, and 10 GPa from right to left.

Figure 6. Predictions of the pressure-induced Raman shifts from the mode Grüneisen tensors (solid black lines) compared to $\Delta\omega/P$ coefficients from literature (colored dotted lines).

Figure 7. Composite rutile + amphibole inclusions in garnet (eclogite from Pohorje massif). (a), (b) – parallel polarized light (PPL) and crossed polarized light (XPL) microphotographs of the inclusions with the surrounding birefringent halo. (c), (d) – Surface inclusion in garnet (XPL and reflected light (RL) microphotographs). Birefringent halo is absent on the image (c) because the stress is released as the inclusion is exposed (see Campomenosi et al. 2018 for details).

Figure 8. Raman imaging of a mixed rutile+amphibole inclusion along XZ and YZ planes. The blue area in the image indicate the presence of the 671 cm^{-1} characteristic peak of amphibole, while dark red and grey are related to the characteristic peaks at 141.6 and 917 cm^{-1} from rutile and garnet, respectively.

Figure 9. Bulk modulus (red) and P_{inc} (orange and green) curves at room conditions of rutile plus cummingtonite mixtures as a function of volume fraction of the amphibole. Negative P_{inc} values are indicated with blue dots, while positive values with red and yellow dots. The bulk modulus curve corresponds to the Reuss expression for the bulk modulus of the two-phase mixture. Values of the P_{inc} are calculated for the entrapment condition at 3 GPa 800°C and at 2 GPa 600°C as an example. The volume fraction of the amphibole (0.14) leading to a zero P_{inc} is also the composition for which the bulk modulus of the inclusion is equal to that of the pyrope host.

591

Tables

592

Table 1. Lattice parameters, atomic coordinates, bonds and angles of rutile

	This work	a	b	c	d	e	f	tw- b
T **(K)**	0	0	15	298	298	298	300	-
				Lattice parameters				
a **(Å)**	4.59867	4.572	4.58666(4)	4.594	4.5924(2)	4.5923(3)	4.499	0.01201
c **(Å)**	2.95652	2.943	2.95407(3)	2.959	2.9575(2)	2.9576(3)	3.077	0.00245
V **(Å^3)**	62.52389	61.52	62.15	62.432	62.38(1)	62.37	62.28	0.37389
				Atomic coordinates				
O_x	0.30485	0.30400	0.30469(6)	0.30500	0.30499(8)	0.3092(6)	0.30590	0.00016
				Bonds and angles				
Ti-O_a (Å)	1.9483	-	1.9459 (3)	-	1.9470(2)	1.930(3)	-	0.0024
Ti-O_b (Å)	1.9826	-	1.9764 (4)	-	1.9808(3)	2.008(4)	-	0.0062
Ti-O-Ti (°)	130.648	-	130.62 (1)	-	130.58 (1)	129.97(9)	-	0.028
O_a-Ti-O_a (°)	81.296	-	81.24 (2)	-	81.16(1)	79.93(18)	-	0.055
Ti-O-Ti (°)	98.704	-	98.76 (2)	-	-	-	-	-0.055
O_b-Ti-O_b (°)	98.704	-	98.76 (2)	-	-	-	-	-0.055

Notes: [a] Mitev et al. 2010, [b] Burdett et al. 1987, [c] Abrahams and Bernstein 1971, [d] Sugiyama and Takéuchi 2015, [e] Henderson et al. 2009, [f] Lan et al. 2015.

593

594

Table 2. Frequencies (cm^{-1}) of the Raman-active modes of rutile.

		This work		a	b	c	d	e	f
		calc	exp	theoretical			experimental		
			Pohorje						
T (K)		0	298	0	0	300	298	298	298
Symmetry	B_{1g}	163.98	141.6	137.0	130.0	169.0	143.0	143.0	143.0
	E_g	453.83	445.28	463.2	457.0	400.0	450.0	449.0	447.0
	A_{1g}	600.03	609.32	611.6	601.0	558.0	612.0	612.0	612.0
	B_{2g}	818.96	801.79	824.7	805.0	803.0	826.0	826.0	826.0

Notes: [a] Montanari and Harrison 2002, [b] Mitev et al. 2010, [c] Lan et al. 2012, [d] Samara and Peercy 1973, [e] Merle et al. 1980, [f] Porto et al. 1967.

595

596

Table 3. Symmetry-independent components of the Grüneisen tensors of rutile at 300K

	ω_0	γ_1	γ_3
B_{1g}	141.6	-5.64 (16)	-4.23(21)
E_g	445.28	1.45 (2)	2.38 (2)
A_{1g}	609.32	1.57 (3)	1.88 (4)
B_{2g}	801.79	1.57 (1)	1.32 (1)

597

Figure 1

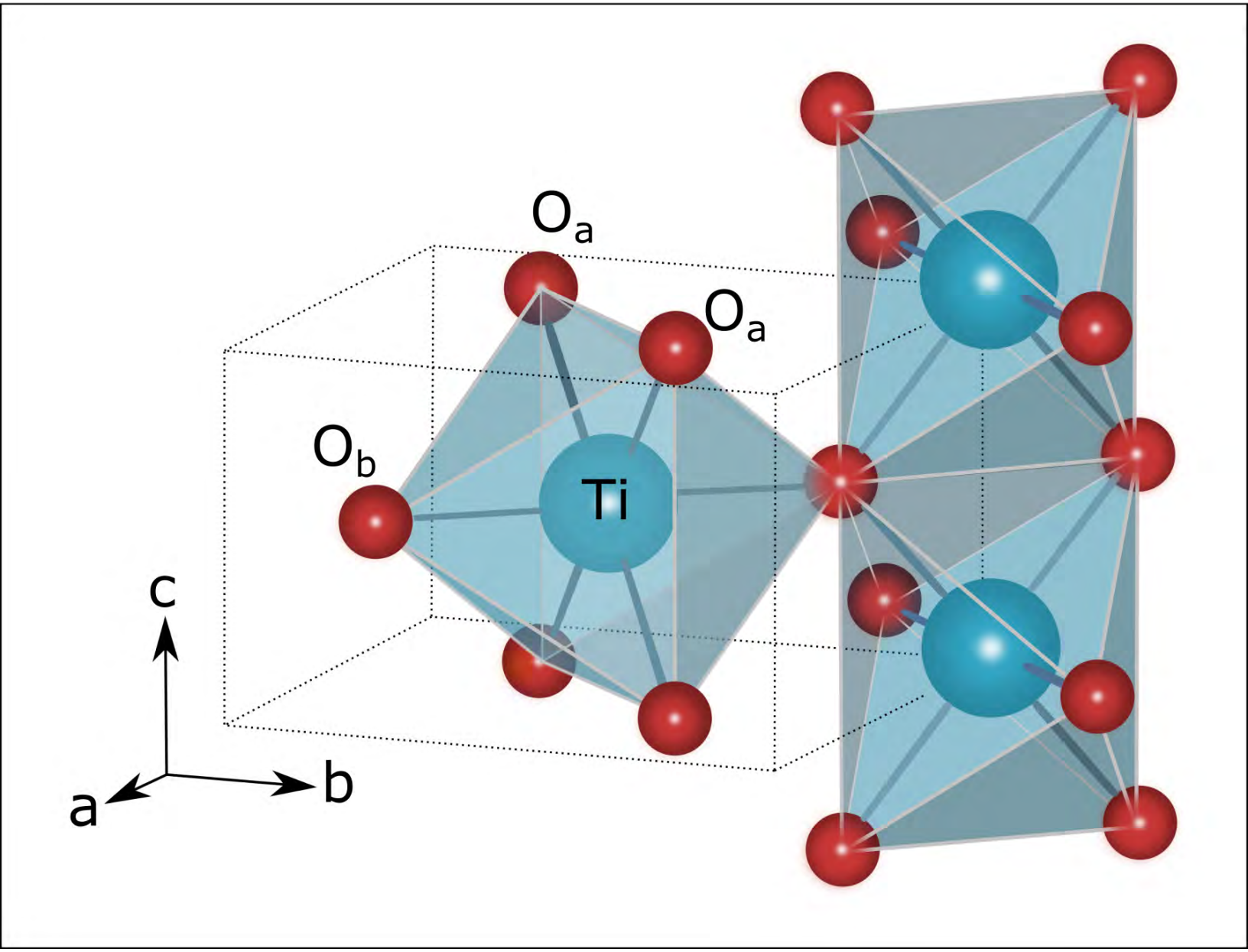

Figure 2

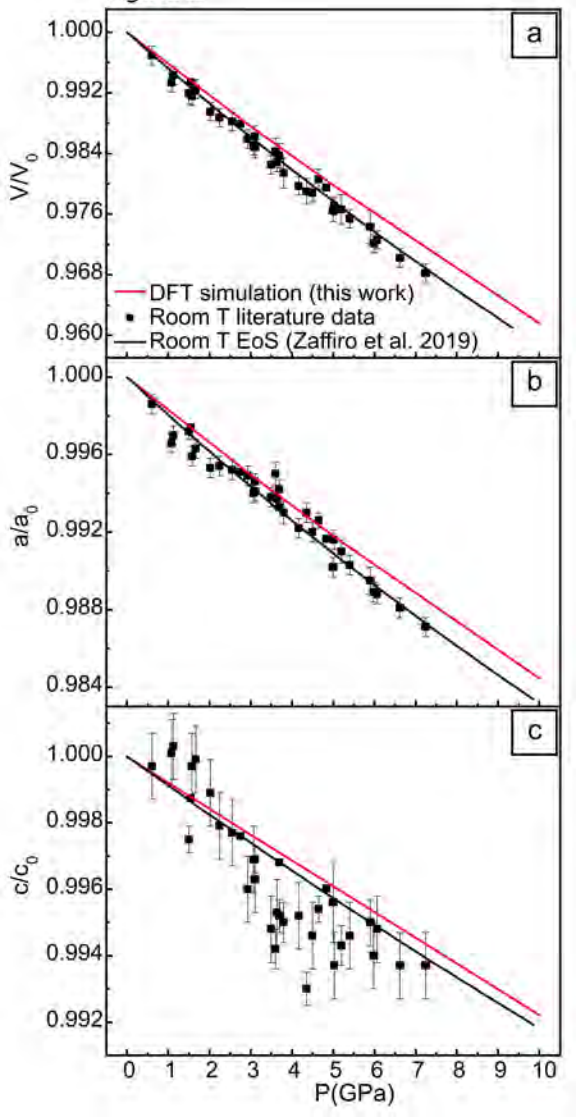
a
b
c
V/V0
a/a0
c/c0
DFT simulation (this work)
Room T literature data
Room T EoS (Zaffiro et al. 2019)
P(GPa)

Figure 3

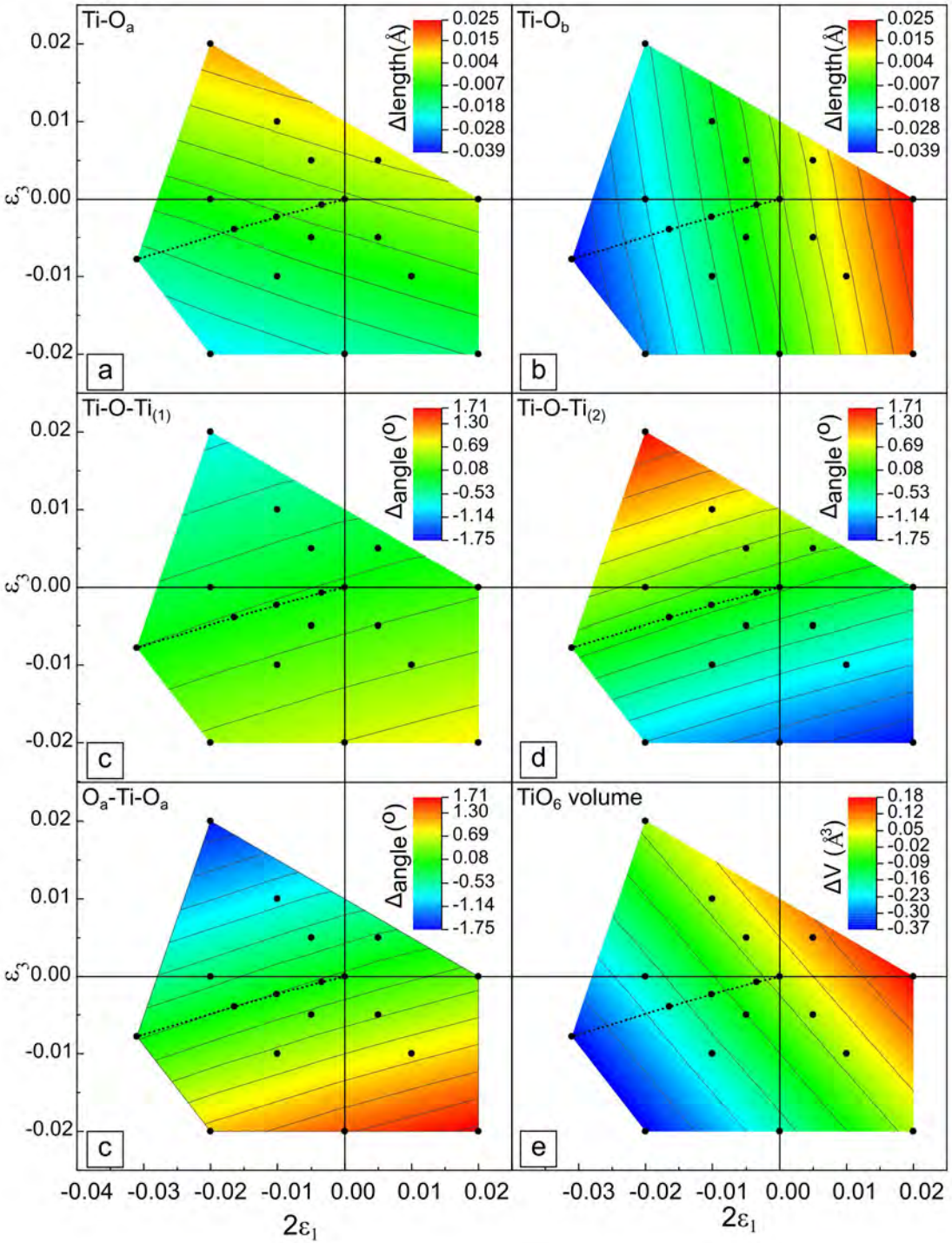
Ti-O$_a$
Δlength(Å)
0.025
0.015
0.004
-0.007
-0.018
-0.028
-0.039
a
Ti-O$_b$
Δlength(Å)
0.025
0.015
0.004
-0.007
-0.018
-0.028
-0.039
b
Ti-O-Ti$_{(1)}$
Δangle (°)
1.71
1.30
0.69
0.08
-0.53
-1.14
-1.75
c
Ti-O-Ti$_{(2)}$
Δangle (°)
1.71
1.30
0.69
0.08
-0.53
-1.14
-1.75
d
O$_a$-Ti-O$_a$
Δangle (°)
1.71
1.30
0.69
0.08
-0.53
-1.14
-1.75
c
TiO$_6$ volume
ΔV (Å^3)
0.18
0.12
0.05
-0.02
-0.09
-0.16
-0.23
-0.30
-0.37
e
ε$_3$
0.02
0.01
0.00
-0.01
-0.02
-0.04 -0.03 -0.02 -0.01 0.00 0.01 0.02
2ε$_1$

Figure 4

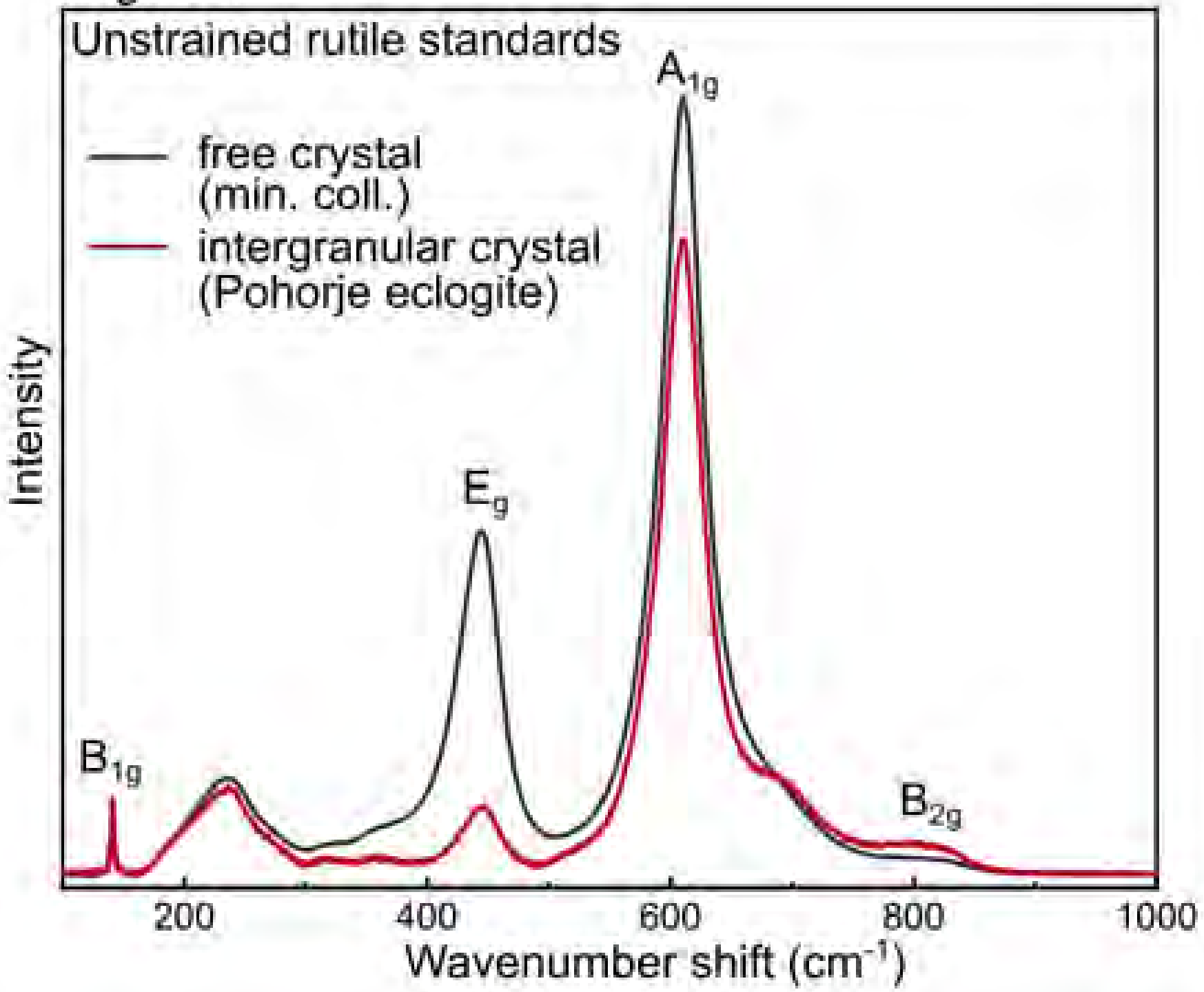
Unstrained rutile standards
free crystal
(min. coll.)
intergranular crystal
(Pohorje eclogite)
A1g
Eg
B1g
B2g
Intensity
200
400
600
800
1000
Wavenumber shift (cm-1)

Figure 5

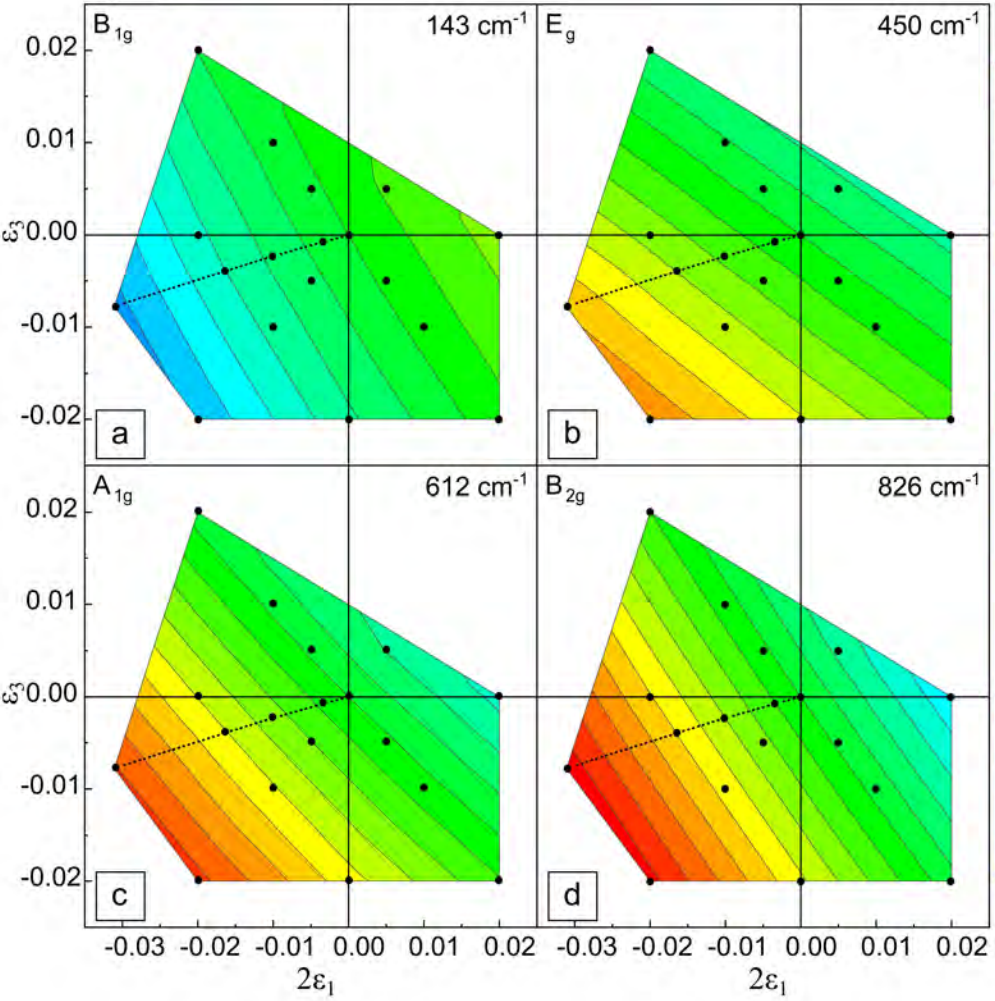
B1g
143 cm-1
Eg
450 cm-1
A1g
612 cm-1
B2g
826 cm-1
a
b
c
d
Δω
50
45
40
35
30
25
20
15
10
5
0
-5
-10
-15
-20
-25
-30
-35
-40
-45
-50
0.02
0.01
0.00
-0.01
-0.02
ε3
-0.03 -0.02 -0.01 0.00 0.01 0.02
2ε1

Figure 6

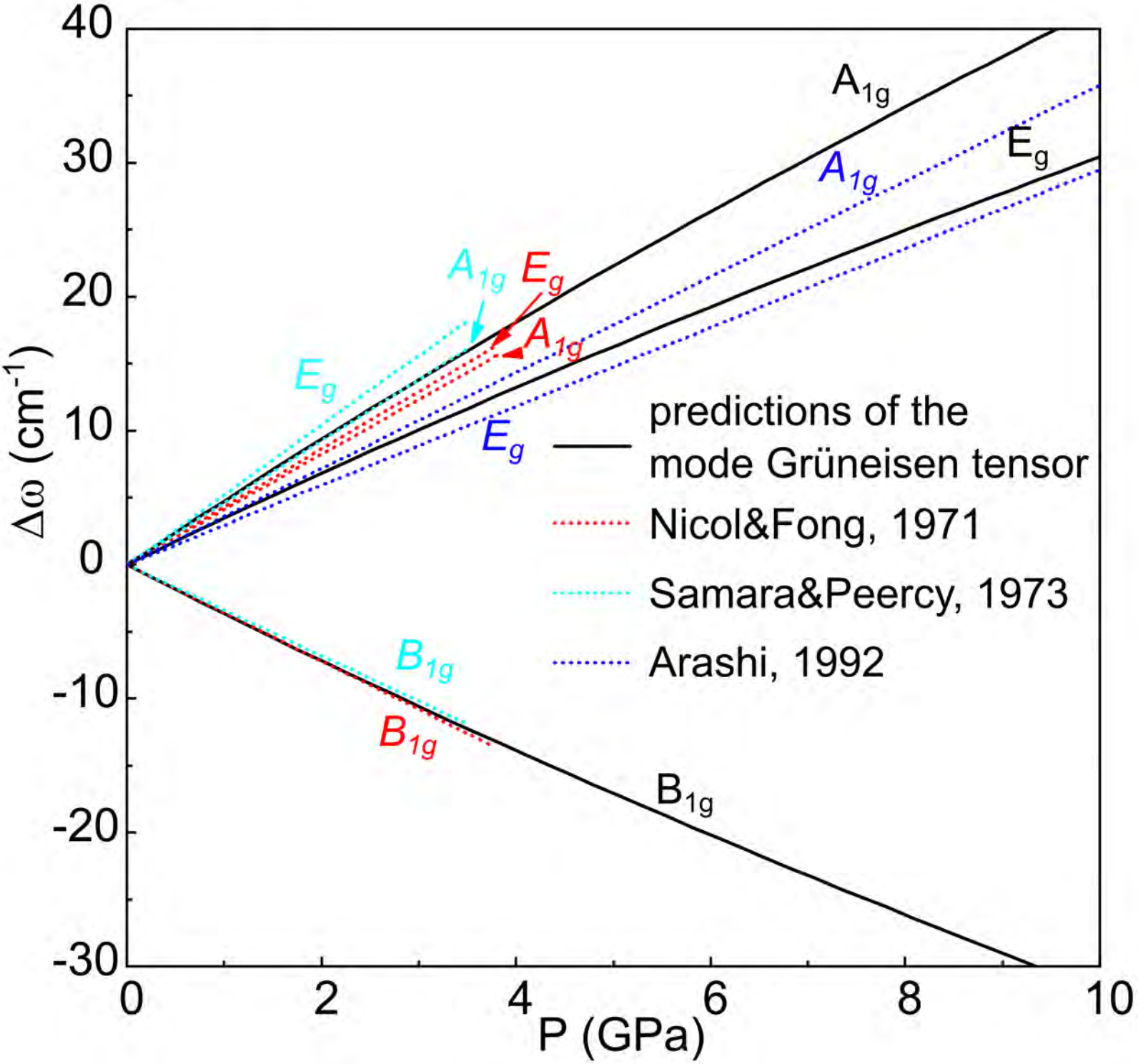
40
30
20
10
0
-10
-20
-30
Δω (cm-1)
0
2
4
6
8
10
P (GPa)
A1g
Eg
A1g
A1g
Eg
Eg
Eg
A1g
B1g
B1g
B1g
predictions of the
mode Grüneisen tensor
Nicol&Fong, 1971
Samara&Peercy, 1973
Arashi, 1992

Figure 7

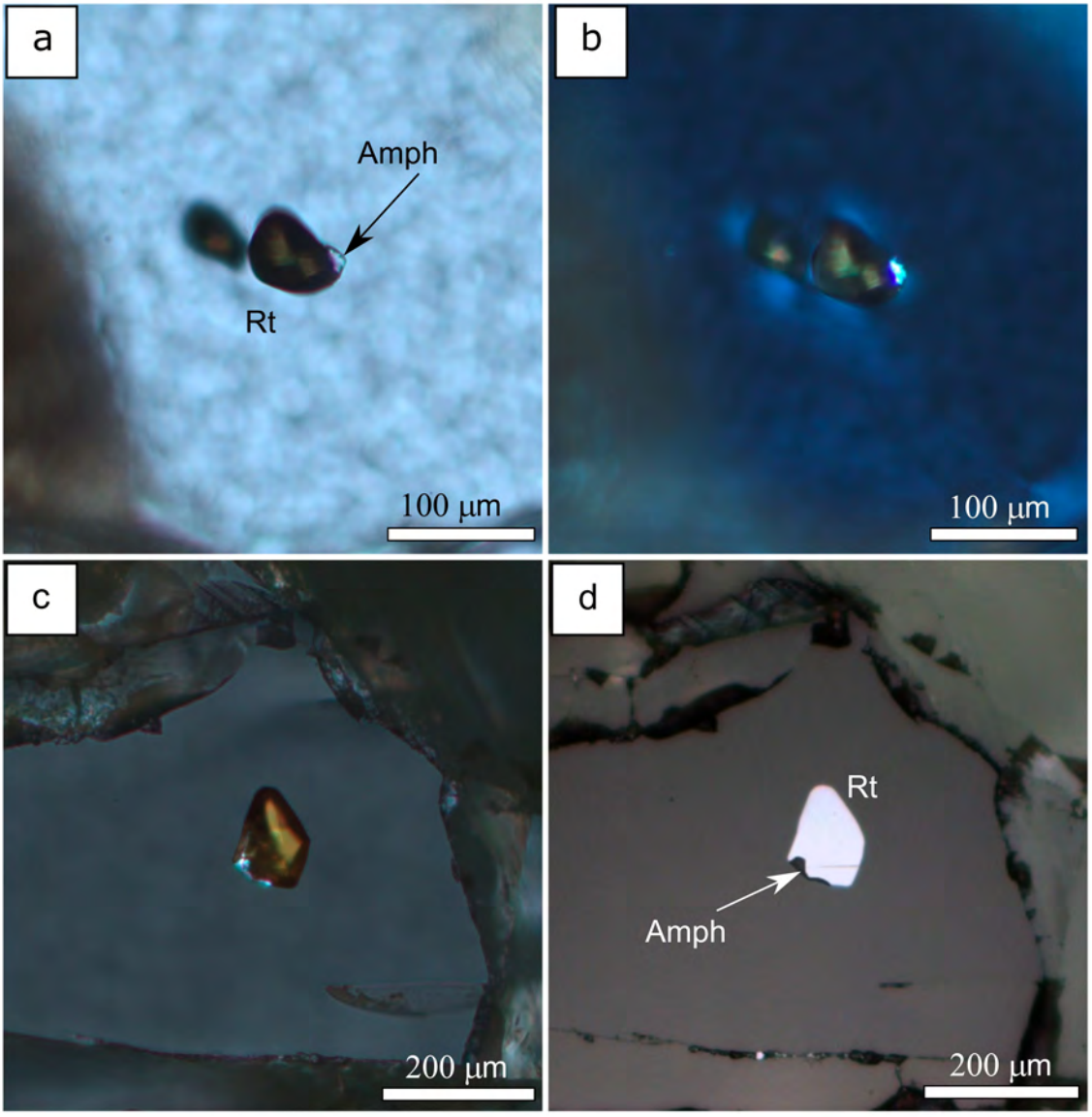

Figure 8

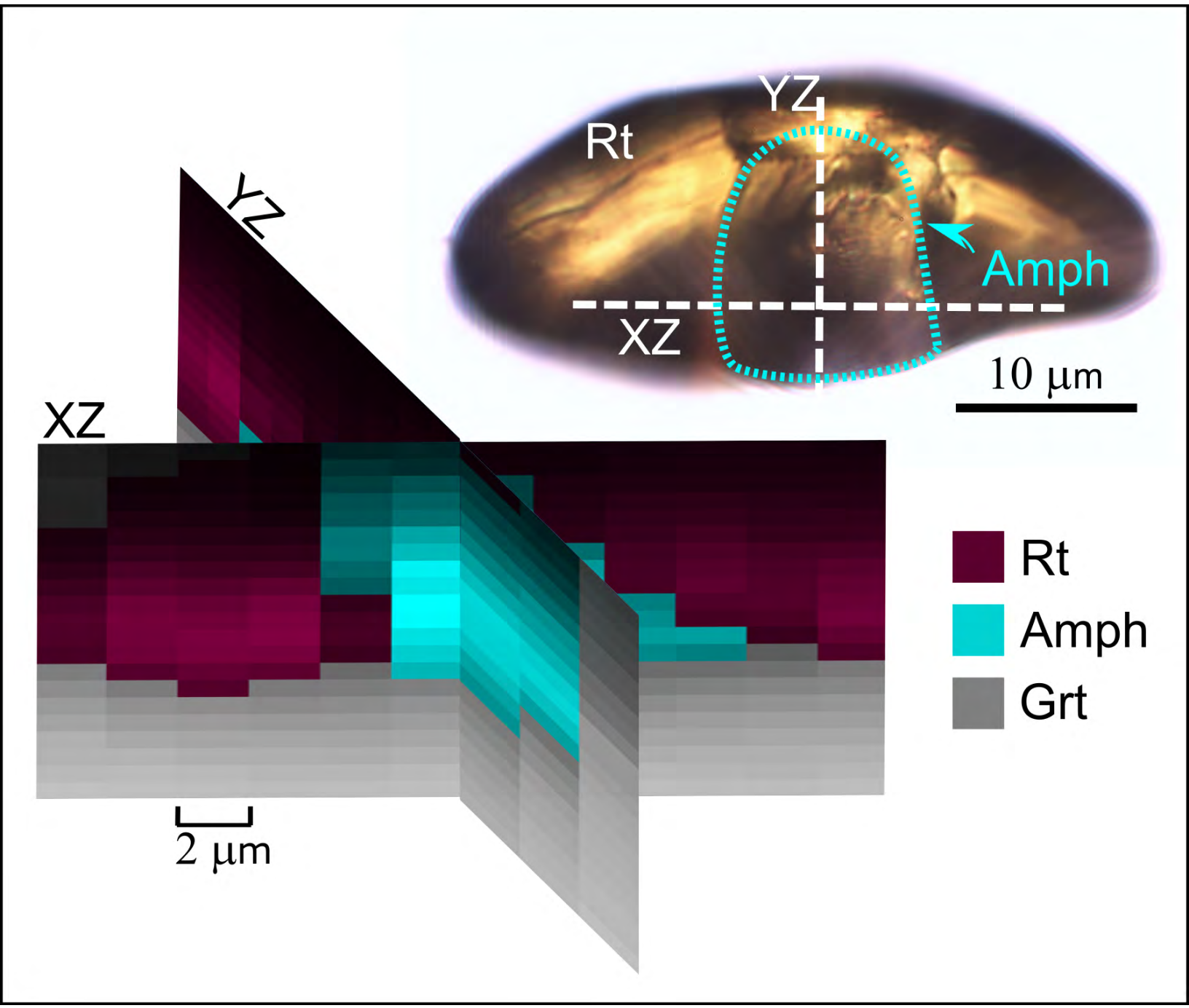

Figure 9

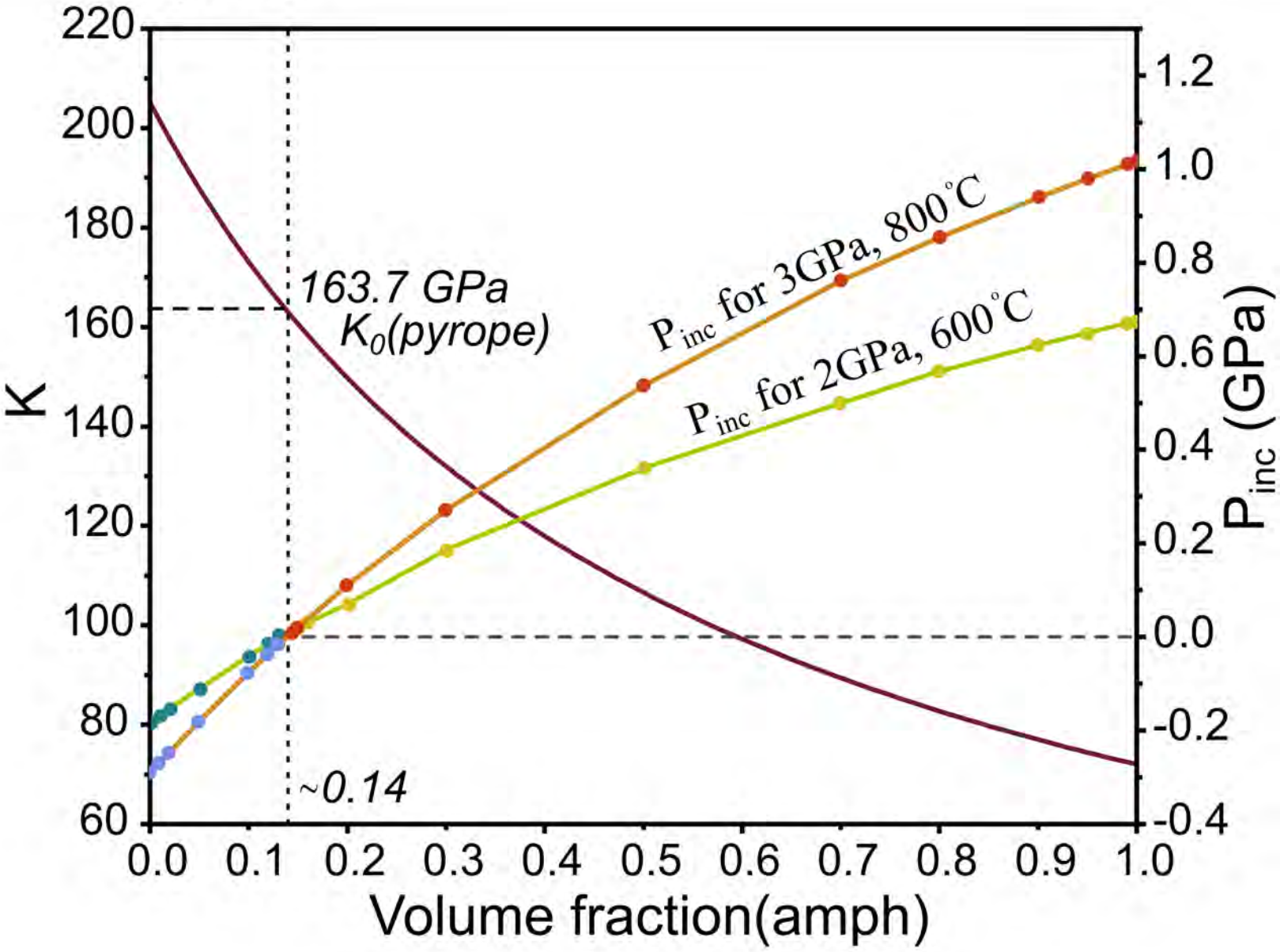
220
200
180
160
140
120
100
80
60
K
163.7 GPa
K_0(pyrope)
~0.14
P_{inc} for 3GPa, 800°C
P_{inc} for 2GPa, 600°C
1.2
1.0
0.8
0.6
0.4
0.2
0.0
-0.2
-0.4
P_{inc} (GPa)
0.0 0.1 0.2 0.3 0.4 0.5 0.6 0.7 0.8 0.9 1.0
Volume fraction(amph)